The impact of porosity and crack density on the elasticity, strength and friction of cohesive granular materials: Insights from DEM modelling

Martin P.J. Schöpfer[*,1], Steffen Abe[+,2], Conrad Childs[1] and John J. Walsh[1]

[1] *Fault Analysis Group, School of Geological Sciences, University College Dublin, Belfield, Dublin 4, Ireland.*

[2] *Seismology & Computational Rock Physics Laboratory, School of Geological Sciences, University College Dublin, Belfield, Dublin 4, Ireland.*

Abstract

Empirical rock properties and continuum mechanics provide a basis for defining relationships between a variety of mechanical properties, such as strength, friction angle, Young's modulus, Poisson's ratio, on the one hand and both porosity and crack density, on the other. This study uses the Discrete Element Method (DEM), in which rock is represented by bonded, spherical particles, to investigate the dependence of elasticity, strength and friction angle on porosity and crack density. A series of confined triaxial extension and compression tests was performed on samples that were generated with different particle packing methods, characterised by differing particle size distributions and porosities, and with different proportions of pre-existing cracks, or uncemented grain contacts, modelled as non-bonded contacts. The 3D DEM model results demonstrate that the friction angle decreases (almost) linearly with increasing

[*] Corresponding author. Tel.: +353 1 7162611; fax: +353 1 7162607

E-mail address: martin@fag.ucd.ie

[+] Present address: Geologie-Endogene Dynamik, RWTH Aachen University, Aachen, Germany

porosity and is independent of particle size distribution. Young's modulus, strength and the ratio of unconfined compressive strength to tensile strength (UCS/T) also decrease with increasing porosity, whereas Poisson's ratio is (almost) porosity independent. The pre-eminent control on UCS/T is however the proportion of bonded contacts, suggesting that UCS/T increases with increasing crack density. Young's modulus and strength decrease, while Poisson's ratio increases with increasing crack density. The modelling results replicate a wide range of empirical relationships observed in rocks and underpin improved methods for the calibration of DEM model materials.

Keywords: Discrete Element Method; Particle Flow Code; Porosity; Friction; Failure envelope;

1 Introduction

Knowledge of the mechanical properties of rocks is fundamental for both Earth scientists and engineers. Failure envelopes and elastic parameters are crucial for modelling a wide range of geomechanical problems, including wellbore failure, slope stabilities and the stability of underground excavations [1]. Rock properties are obtained from in-situ tests and more commonly in the laboratory from samples that are loaded using stress and/or displacement controlled experiments. These tests have given many insights into the behaviour of rock and have shown, for example, that the elastic parameters and strength depend on porosity and cement content, though the details of these dependencies are also partly controlled by mineral composition (e.g. carbonate vs siliciclastic rocks; [2,3]). Obtaining core samples from depth for laboratory testing is both time-consuming and expensive. Hence rock physical properties are often estimated using empirical relations, such as the correlation between Young’s modulus and sonic velocity, or that between unconfined compressive strength and porosity [4]. Rock is, however, a heterogeneous material and even multiple samples obtained from a single slab of rock can exhibit significant compositional variability and hence mechanical behaviour [3]. Therefore some of the above mentioned empirical rock property relations are poorly constrained. One of the principal aims of this work is to investigate these empirical property relations in numerical rock analogues where the effects of compositional heterogeneity can be isolated.

Numerical modelling offers a new avenue to better understand material property relations. An advantage of numerical modelling is that the user can examine systematically the effect of varying individual input parameters while keeping all other parameters constant; this is rarely possible with laboratory measurement. The

Discrete Element Method (DEM), where rock is represented as an assemblage of particles (spheres, ellipsoids, blocks) that interact with each other, is ideal for investigating mechanical property relations since the user predefines microproperties (particle and cement properties) and determines macroproperties (elastic and strength parameters) using numerical lab experiments [5]. The mechanical behaviour of the model material is not predefined, as in continuum approaches, but emerges from the interaction of particles and cement [6].

The aim of this study is to investigate the impact of particle size distribution, porosity and cement content (i.e. proportion of bonded contacts) on the mechanical properties (elasticity, strength, ratio of unconfined compressive strength to tensile strength and friction angle) of DEM model materials in 3D. In the next section we provide a brief review of rock property relations which are relevant for this study. In the following sections we describe the results of the various numerical mechanical experiments conducted on samples generated using a range different packing methods and compare the observed failure envelopes, failure criteria and rock mechanical property relations (cement content, porosity) with those of rocks.

2 Rock property relations and failure envelopes

In this study we numerically investigate relations between porosity, cement content and rock mechanical properties. Here we summarise the most important empirical relations obtained from lab experiments (see Fig. 1), which provide the essential backdrop to the numerical modelling presented in Section 4.

Probably the most commonly used failure criterion for rock is the Coulomb criterion, which, expressed in terms of the principal stresses σ_1 and σ_3 ($\sigma_1 > \sigma_3$ and compressive stresses positive throughout this paper), is written as

$$\sigma_1 = \mathrm{UCS} + \sigma_3 \tan^2(45° + \varphi_i / 2), \tag{1}$$

where UCS is the unconfined compressive strength and φ_i is the angle of internal friction, the tangent of which is called the coefficient of internal friction μ_i [1]. Experimental data and theoretical models [7] suggest, however, that a linear failure criterion is only valid over a limited range of confining pressures and that a non-linear failure envelope concave towards the minimum principal stress axis (in a σ_1 vs σ_3 plot) may prove to be the rule rather the exception [2]. An additional limitation of both linear and non-linear failure criteria is that they are often independent of the intermediate principal stress, σ_2 (Mohr criteria), whereas data from polyaxial tests suggests that many rock types exhibit a σ_2 dependence of strength [3,8]. Consequently peak stress data and associated failure envelopes obtained from triaxial extension and triaxial compression tests exhibit a mismatch, where the former plots above the latter in a σ_1 vs σ_3 plot (Fig. 1a). Under some circumstances this mismatch can be eliminated by using a criterion that takes the impact of σ_2 into account (Fig. 1b). Finally very few experimental data exist within the tensile field (σ_3 < 0; Fig. 1a) to define the transition from tensile to shear failure [9], though a parabolic failure envelope is most commonly used [10].

Laboratory tests of rocks indicate that strength, angle of internal friction and Young's modulus decrease with increasing porosity ([4,11-14]; Fig. 1c, d and e). Additionally the presence of pre-existing cracks, which have been simulated in the laboratory by cyclically heating the rock specimen before loading [15,16], has a significant impact on rock mechanical properties (Fig. 1f, g and h). For example, strength, the unconfined compressive strength, tensile strength (UCS/T) and Young's modulus decrease with increasing number of heating cycles, which can be related to the proportion of non-cohesive grain-grain contacts or crack density.

3 Methods

3.1 *Discrete Element Method*

The results in this paper have been obtained using two different 3D implementations of the DEM for spherical particles, the Particle Flow Code (PFC3D; [5,17]) and ESyS-Particle (formerly LSMearth; [18,19]). Both codes implement a linear force-displacement contact law with Coulomb friction and a particle-particle bond model that transmits both force and moment. The majority of the results presented in this paper were obtained using PFC3D and the microproperties used are given in Table 1. The details of the contact and bond law implementation are slightly different in ESyS-Particle, hence only UCS/T ratios are given and compared to those obtained from PFC3D.

As stated earlier, in a DEM model microproperties are defined and the macroproperties are obtained using numerical lab experiments, details of which are given in Section 3.3. The user therefore varies the microproperties systematically until the material exhibits the desired macroscopic mechanical behaviour. There are, however, two problems with calibrating DEM models consisting of spherical particles to match the response of real rock: (i) The (internal) friction angle of both cohesive and non-cohesive materials is typically too low, irrespective of the contact (i.e. particle-particle) friction coefficient [20]. Previous attempts to increase the friction angle have included modifications to the standard DEM approach including the use of clumped [5,21,22] or elliptical particles [23], implementing a rolling resistance [24] and explicitly prescribing the macroscopic failure criterion using hybrid methods [25].

(ii) The ratio of unconfined compressive strength to tensile strength (UCS/T) of DEM models of cohesive rock is too low (*ca* 3-4) compared to rock (> 10), an issue that has only recently been addressed in 2D [22,26]. We show later that both the low friction angles and low UCS/T ratios obtained in previous studies were partly a consequence of the particle packing methods used, which lead to porosities that were too high to achieve realistic properties without modifying the standard DEM. In this study, we show that different particle packing methods, and hence different particle size distribution and model porosity, combined with different proportions of bonded contacts can replicate the range of friction angles and UCS/T ratios associated with rocks.

3.2 *Model Generation and Packing Methods*

There are two end-member methods for generating random dense packing of spheres for DEM simulations, constructive and dynamic [27]. For this study we used one constructive method, the particle insertion method [28], one dynamic method, the specimen genesis procedure widely used by PFC3D users [5], and a hybrid of these two (Fig. 2).

The dynamic specimen genesis procedure used for this study, which is described in detail in Ref. 5, is based on a four-step process. (i) Particles with radii chosen randomly from a uniform size distribution are randomly generated within a volume bound by planar, frictionless walls. (ii) The system is allowed to adjust by particle movement under zero friction. (iii) A low isotropic stress is installed by modifying the radii of all particles simultaneously. (iv) The radii of particles that have less than three contacts are modified iteratively, so that these particles have at least three contacts (over 99% of particles have 4 or more contacts in the final model) and their mean contact normal force is low in relation to the mean contact force of the assembly. Models generated with the dynamic method had a uniform PSD with r_{max}/r_{min} of 1.66 (Fig. 3) and a porosity of ~37% (model i in Fig. 2).

For the particle insertion method ‘seed’ particles are first generated within the specimen domain. The specimen is then filled up by iteratively inserting particles so that each new particle touches four neighbours. The filling-up of the specimen is completed when no further particles can be inserted. The number of particles and the final porosity that can be achieved with this method are a function of the predefined particle size range (r_{max}/r_{min}). Models generated with the particle insertion method had a power-law particle size distribution (PSD) with an exponent of ~3.0 (Fig. 3) and a porosity of ~23% if the maximum to minimum particle radius ratio (r_{max}/r_{min}) is 10 (model ii in Fig. 2).

Porosities between 23 and 37% were achieved in three different ways (Fig. 2): (i) systematic deletion of the smallest particles from a power-law PSD model with 23% porosity (2^{nd} row in Fig. 2), (ii) direct generation of an assembly with power-law PSD using $r_{max}/r_{min} < 10$, and (iii) insertion of particles into a uniform PSD assembly with an initial porosity of 37% using the particle insertion method referred to above (1^{st} row in Fig. 2). All specimens were rectangular parallelepipeds with a square base and a height to width ratio of 2.

The average coordination numbers (i.e. number of contacts per particle) of the models range from 7.3 to 5.8, where the low porosity models have both a greater average and a greater range of coordination numbers. The average coordination numbers of the different PSD models are almost identical (within 10%) for a given porosity, though the range of coordination numbers is greater in the power-law PSD models than in the uniform/bimodal PSD models. For example, the greatest coordination number in the 23% porosity power-law model is 131, whereas in the bimodal model with identical porosity it is 56. The mode of coordination numbers in all models is 4 (which is the value for a newly inserted particle in the particle insertion method explained above), except in the 37% porosity model with uniform PSD, in which the mode is 5. In summary, the average coordination numbers decrease slightly, whereas the range of coordination numbers decreases significantly with increasing porosity. A possible explanation for the observed relationship between mechanical properties and porosity is that the reduction in the number of contacts which accompanies an increase in porosity gives rise to an increase in the tortuosity of remaining force chains, causing a decrease in Young's modulus, and an increase in the load they transmit causing a decrease in sample strength.

While the model porosity values cannot be compared directly to those of real rocks, which are typically composed of non-spherical grains that can be packed better than spheres, and the effect of finite sized cement using bonds was not taken into account in the porosity calculations, the model results provide a means of exploring general mechanical consequences of porosity changes and cementation.

3.3 *Compression and Extension* T*ests*

Confined triaxial compression tests ($\sigma_1 > \sigma_2 = \sigma_3$) were performed by shortening the specimen along its long axis with top and bottom platens using a constant velocity that is slow enough to ensure quasi-static conditions, whilst maintaining a constant confining pressure between 0.1 and 40 MPa using servo-controlled lateral platens. The failure envelopes were constructed using the peak stress (σ_1) value of the stress strain curve at a given confining pressure (σ_3) and the angle of (internal) friction was calculated from the slope of the principal stress data (Eq.1).

Confined triaxial extension tests ($\sigma_1 = \sigma_2 > \sigma_3$) were performed using particles to apply boundary forces and velocities. The sample was first confined to the desired confining pressure using servo-controlled platens. Then particles touching the platens are identified, the platens are removed, one calculation cycle is performed, and the out-of-balance forces of the boundary particles are replaced by applied forces with the same magnitude but opposite direction. Particles of the upper and lower 10% of the sample are then combined to form two non-breakable clumps which are then pulled apart while the lateral forces are kept constant. Since a velocity is applied to all particles within the upper and lower portions of the model, stress concentrations that would arise if the model would be extended using clamps are eliminated. The stableness of the boundary condition used is supported by the fact that macroscopic failure never occurred along the edge of the clumps, but within the central part of the model, most likely due to elastic necking. The axial stress (σ_3) is computed by dividing the average out-of-balance force of the clumps by the cross-sectional area of the sample. Preliminary results suggest that comparison of the tensile strength values obtained from the direct tension tests with those derived from Brazilian disc tests is not straightforward, since the Brazilian strength values are sensitive to both disc thickness and the width of the loaded section, and disc failure occurs at the edge of the models, rather than in the centre of the disc, as predicted for materials with low UCS/T values [35].

Young's modulus and Poisson's ratio were obtained from uniaxial strain tests ($e_1 \neq 0$, $e_2 = e_3 = 0$) by fixing the lateral platens and shortening the sample vertically ($e_1 > 0$) until the first bond breakage occurs. The elastic parameters were calculated using the final stresses acting on the platens by [1]

$$\sigma_1 = (\lambda + 2G)e_1, \qquad \tfrac{1}{2}(\sigma_2 + \sigma_3) = \lambda e_1, \tag{2}$$

where λ and G are Lame's constants.

4 Results and Discussion

The models replicate a wide range of behaviours observed in laboratory deformation of rock, in terms of the stress-strain behaviour, the shapes of the failure envelopes and their dependence on the numbers of non-bonded contacts (cracks) and porosity. These aspects of the model results are discussed in sequence in the following sections.

4.1 *Stress-Strain Curves*

Stress difference and volumetric strain (volume decrease taken as negative) vs axial strain curves of the two end-member models (framed in Fig. 2) at various confining pressure are shown in Fig. 4. These curves show a variety of differences in mechanical behaviour between the high and low porosity models. The most obvious difference is that the slopes of the stress-strain curves and the peak stress values are much greater in the low porosity model. The slope of the stress-strain curve of a triaxial compression test is Young's modulus ($d\sigma_1/de_1$ = E) and the slope of the volumetric strain curve is a function of Poisson's ratio ($de_v/de_1 = 2\nu$-1). The curves in Fig. 4 therefore show that, Young's modulus is strongly dependent on porosity, moderately dependent on the percentage of bonded contacts and weakly dependent on confining pressure. The first two dependencies are discussed later; the pressure dependence of Young's modulus is shown in Fig. 5a, together with the results obtained from uniaxial strain tests. Poisson's ratio, however, is only weakly dependent on porosity and the percentage of bonded contacts, but very sensitive to confining pressure. Especially at low confinement, Poisson's ratio is much greater than the values obtained from the uniaxial strain tests (Fig. 5b). This pressure sensitivity of Poisson's ratio is even more pronounced in partially bonded materials, which exhibit volume increase from the onset of axial shortening (dotted curves in Fig. 4b and e), hence Poisson's ratios of >0.5 are obtained. These high values obtained from triaxial compression tests at low confinement are, however, not representative and therefore uniaxial strain test results are given throughout the paper.

The stress-strain curves of the high and low porosity models do share, however, a number of similarities, e.g. the stress-difference and strain at failure increases with increasing confinement (Fig. 4). Additionally, the stress-drop after failure decreases and becomes less abrupt with both, increasing confinement and increasing number of non-bonded contacts, i.e. the material becomes less brittle. It is important to note, however, that Young's modulus, strength and stress-drop can be increased by increasing both the particle stiffness and the bond strength without significantly modifying the friction angle and UCS/T as long as a load-bearing framework exists within the model. In the non-bonded models hardly any stress-drop is observed and these materials deform at an approximately constant stress-difference (although not constant volume) after an initial non-linear stress increase (Fig. 4c and f).

Stress-strain curves obtained from unconfined compression tests on the ten models shown in Fig. 2 are plotted in Fig. 6 (for fully bonded models). These curves illustrate that porosity has a strong impact on both peak stress and Young's modulus. The particle size distribution (uniform/bimodal and power-law, Fig. 6a and b, respectively) has an impact on the elastic properties, where slightly higher Young's moduli and (for low confinement) higher Poisson's ratios are observed in the power-law material. A more quantitative description of these mechanical properties/porosity relations is given in Section 4.5.

4.2 *Shape of Failure Envelopes*

Failure envelopes were constructed using peak stress values (dots in Figs. 4 and 6) and are plotted in principal stress diagrams in Fig. 7. The failure envelopes for the non-bonded materials are straight, i.e. the cohesionless materials exhibit Coulomb-type behaviour. The envelopes obtained from triaxial compression tests on bonded model materials are concave towards the minimum principal stress axis (the data points at $\sigma_3 = 0$ are the UCSs). Therefore, the addition of cohesion (i.e. cement) does not simply shift the straight failure envelope of the non-bonded material towards higher strength (σ_1) values, but also introduces a non-linear pressure strength dependence. As a consequence the angles of internal friction of the various bonded materials decrease non-linearly with increasing confinement, to values which are lower than the interlocking/sliding friction of the non-bonded material (Fig. 7c). Our model results are therefore in agreement with theoretical considerations [7], which suggest that the phenomenon of internal friction and the non-linearity of failure envelopes for rock can be explained by the frictional resistance to sliding offered by the fractured volume that comprises part of the incipient fault plane.

The failure envelopes in the tensile field ($\sigma_3 < 0$) are non-linear and are ‘overturned’ at low confining pressures (Fig. 7a and b). This strengthening effect is neither predicted from critically stressed crack theory (Griffith criterion) nor is it observed in lab experiments on low-porosity, crystalline rock [9,10]. However, an increase in tensile strength at low confining pressures was observed in confined triaxial extension tests on Berea sandstone (ϕ = ~19%; Fig. 1a [29]), which was deformed using the same procedure as described in Ref. 9. The model failure envelopes shown in Fig. 7a and b illustrate that the strengthening effect becomes more pronounced with increasing porosity and increasing percentage of non-bonded contacts suggesting it is confinement related.

The unconfined biaxial strength ($\sigma_1 = \sigma_2 > 0$, $\sigma_3 = 0$), which is the intercept of the triaxial extension failure envelope with the σ_1 axis, is greater than the UCS ($\sigma_1 > 0$, $\sigma_2 = \sigma_3 = 0$). This strength difference is due to a σ_2-dependence of strength; hence Mohr criteria cannot be used for fully describing failure envelopes of cohesive DEM materials, and more complicated criteria that take the effect of the intermediate stress on strength into account need to be considered, details of which are given in the next section.

4.3 *Failure Criterion*

The misfit between the triaxial extension and triaxial compression failure envelopes in Fig. 7a and b indicates that a Mohr criterion, where the maximum principal stress at failure is a function of the minimum principal stress only, can not be used to fit our model data. A variety of polyaxial criteria have been proposed in the past [3,8]: Here we use the Mogi 1967 empirical criterion [30] for quantifying the σ_2-dependence of strength, which is written as

$$(\sigma_1 - \sigma_3)/2 = f[(\sigma_1 + \beta\sigma_2 + \sigma_3)/2], \quad (3)$$

where β is a constant smaller than 1 that reflects the σ_2-dependence in strength, i.e. the criterion reduces to a Mohr criterion if β equals 0. f is some monotonically increasing function; linear, power-law and parabolic functions are the most commonly used. The best-fit to our data was obtained using a parabolic function. Our analysis revealed that the best-fit β-values are independent of the percentage of non-bonded contacts, but are different for the two end-member porosity models, and are 0.19 for the 37% and 0.13 for the 23% porosity models (Fig. 8). Interestingly a parabolic function with a β-value of 0.14 gives a good fit to the triaxial extension and triaxial compression test results of Berea sandstone (ϕ = ~19%; Fig. 1b). Those results provide some indication that porosity has an important control on the β-value. Additionally no polyaxial data, where all principal stresses are different, were used for determining the best-fit failure criterion in this study and it is likely that polyaxial data will reveal that a different criterion to that used here needs to be considered for fully describing the 3D failure envelope of cohesive DEM materials.

4.4 *Impact of Non-Bonded Contacts, or Pre-Existing 'Cracks'*

From the failure envelopes shown in Fig. 7 and 8 it is clear that the strength of the model material not only depends on porosity but also on the relative abundance of non-bonded contacts. These non-bonded contacts could be considered to be analogous to non-cemented grain contacts in rock or perhaps more generally to closed, pre-existing cracks, where sliding occurs if a critical shear stress given by Coulomb friction is exceeded. The percentage of non-bonded contacts, which is the measure used throughout this paper to describe the proportion of cement, is clearly related to crack density as used in micromechanical models [1], but a direct quantitative comparison is difficult and beyond the scope of this study. Although we follow earlier analytical and laboratory studies by describing model results in terms of crack density, a direct link with uncemented grain-grain contacts is more valid (for example, high proportions of uncemented grain contacts are features of poorly lithified sandstones). The model results indicate that the strength of model materials decreases with increasing number of non-bonded contacts (Fig. 9a). Our models also show that the presence of non-bonded contacts has a greater impact on tensile strength than on compressive strength, a feature which reflects the fact that a non-bonded contact can bear some load in compression but no load in tension. Consequently the ratio of unconfined compressive strength to tensile strength (UCS/T) increases with increasing percentage of non-bonded contacts (Fig. 9b). A similar impact of pre-existing cracks on strength and UCS/T for rock was demonstrated in Ref. 16, where an increase of UCS/T from ~20 for intact sandstone to about 50 for sandstone with partially disintegrated grain boundaries is reported (Fig. 1f and g). Most importantly, the UCS/T ratios obtained from only partially bonded model materials are within the range of those described for rock, which tend to have strength ratios of ~10 [1].

Fig. 9b shows that UCS/T also depends on model porosity, with higher UCS/T values obtained for lower porosity materials. The similarity between the UCS/T ratios for the 37% porosity PFC3D material used in this study and the 35% porosity model of Lac du Bonnet granite (see caption) with very different microproperties and sample shape is consistent with porosity exerting a significant control on UCS/T. The ESyS data show that UCS/T is, for the range of model sizes tested in this study, basically independent of model resolution. Low porosity (22-23%) PFC3D and ESyS data, apart from the fully bonded PFC3D model, exhibit identical ratios and trends, which suggests that the details of the contact and bond implementations have only marginal affects on UCS/T ratios of models with more than ca 10% non-bonded contacts. Significant differences of UCS/T for the fully bonded low-porosity models are only weakly dependent on porosity (Fig. 10b) and therefore must reflect sensitivities in mechanical behaviour due to contact/bond implementations.

The presence of non-bonded contacts also has an impact on the elastic properties (Fig. 9c): Young's modulus (E) decreases whereas Poisson's ratio (ν) increases with increasing percentage of non-bonded contacts. These general trends are also predicted by various micromechanical models for linear elastic materials containing randomly oriented, closed cracks (e.g. chapter 10 in Ref. 1) and similar relations were observed in cyclic loading experiments on granite [31], and experiments on sandstone with partially disintegrated grain boundaries (Fig. 1h; [16]).

4.5 *Porosity Relations*

Both tensile strength (T) and unconfined compressive strength (UCS) decrease with increasing porosity and are basically independent of the PSD (Fig. 10a). This decrease in strength with increasing porosity is consistent with empirical rock property relations (Fig. 1c; [4]). In the models UCS, however, decreases more rapidly than T, and consequently UCS/T decreases with increasing porosity (Fig. 10b). The UCS/T ratios of the ESyS models exhibit a similar relation, though the ratios are, for a given porosity, greater than those obtained from PFC3D models, and also decrease more rapidly with increasing porosity (Fig. 10b). We believe that these results reflect the differences of the bond model implementations in PFC3D and ESyS.

The friction angles for non-bonded materials with various PSDs and porosities are shown in Fig. 10c together with the range of internal friction angles determined for the fully bonded end-member models (Fig. 7c). The friction angles for the non-bonded materials decrease (almost) linearly with increasing porosity and are (almost) independent of the PSD (Fig. 10c). The internal friction angles suggest a similar relation, though the scatter is significant due to non-linearity of the failure envelopes, especially at low confining pressures. Nevertheless, this general trend has also been described for natural rock (Fig. 1d; [4,14]). We believe that the decrease in friction angles with increasing porosity is due to a decrease of internal roughness, though future micromechanical studies are necessary to fully understand the relation of the angle of (internal) friction with porosity.

Young's modulus decreases significantly with increasing porosity, though the modulus is greater for the power-law than for the uniform and bimodal PSD models (Fig. 10d). Poisson's ratio is (almost) independent of porosity, but higher for the uniform/bimodal than the power-law PSD models. The decrease in Young's modulus with increasing porosity and the porosity-independence of Poisson's ratio are consistent with micromechanical models [1], with data obtained from continuum method models [32], and with empirical rock property relations (Fig. 1e; [4]).

Finally, as stated earlier, some of the Young's modulus and strength values of the model materials are greater than those for real rock. However, since E and UCS (and T) are proportional to particle and bond stiffnesses, and to bond strengths, respectively, calibration of the model material to that of real rock (e.g. sandstone) should be straightforward and will be the aim of future studies.

5 Summary and Conclusions

The mechanical properties of rock and other materials are strongly dependent on porosity and crack density. In this study we investigate some of these dependencies using the Discrete Element Method (DEM) in 3D and a selection of results is shown in Fig. 11. Young's modulus, strength, UCS/T and angle of (internal) friction decrease with increasing porosity. The elastic constants, however, also depend on confining pressure, where Young's modulus and Poisson's ratio increase and decrease with increasing pressure, respectively. The failure envelopes of the cohesive materials are non-linear and the observed misfit between triaxial extension and compression envelopes is due to a σ_2-dependence in strength, which is more pronounced in the high porosity materials. Young's modulus, strength and UCS/T decrease whereas Poisson's ratio increases with decreasing cement content (increasing 'crack' density).

While we have not attempted to match the range of properties of any particular rock, our numerical test results replicate both qualitatively and quantitatively the range of mechanical behaviours observed for brittle rock. Perhaps most importantly, by varying porosity and the proportion of bonded contacts in DEM materials comprised of spherical particles, it is possible to achieve the high UCS/T ratios and the range of angles of internal friction that are observed in rocks. These high UCS/T ratios and friction angles were previously only reproducible by modifying the DEM (using irregular shaped particles, or implementing rolling resistance).

Many low-porosity, crystalline rocks exhibit UCS/T ratios greater than 10, i.e. greater than those achieved using the particle and bond properties of the present study. Although UCS/T > 10 can be easily achieved by using a greater proportion of non-bonded contacts (Fig. 9b), the stress and especially the volumetric strain behaviour becomes less similar to that observed in brittle rock (though, as expected, the behaviour does match that of poorly lithified, granular materials). In low-porosity crystalline rocks that exhibit UCS/T >10, grain interlocking and the resistance to grain rolling are important mechanisms that increase both friction and UCS/T. Hence it might be necessary to use irregular shaped particles or a particle rolling resistance method for modelling such low-porosity rocks. These methods have, however, associated disadvantages, for example the lateral strains are not matched if unbreakable clumps are used [5, 22]. The decision as to whether to use these approaches or the methods outlined in this article depends on which aspects of the rock mechanical behaviour need to be captured in the model.

Our study highlights the fact that both porosity and the proportion of bonded contacts (crack density) are important parameters that should be considered during the calibration of DEM materials to rocks. Including these two parameters provides a means of modelling a wider range of rock types than was previously possible [33]. The relationships we observed between these two parameters and a range of mechanical properties closely replicate the equivalent relationships determined experimentally for rocks.

Acknowledgments

Childs, Schöpfer and Walsh acknowledge funding from a Science Foundation Ireland (SFI) grant, an Irish Research Council for Science, Engineering and Technology (IRCSET) Embark initiative postdoctoral research grant and financial support from ExxonMobil and Shell. Abe acknowledges funding from the EU-SPICE project. Abe's ESyS simulations were performed on the computing cluster of the Seismology & Computational Rock Physics Laboratory at University College Dublin. Stimulating discussions with P. Cundall, M. Pierce and D. Potyondy (HCItasca) and T. Manzocchi (Fault Analysis Group) are gratefully acknowledged. Constructive comments of two anonymous reviewers and the editorial advice of R. Zimmerman are acknowledged.

References

[1] Jaeger JC, Cook NGW, Zimmerman RW. Fundamentals of rock mechanics. 4^{th} edition, Blackwell Publishing, Oxford, 2007.

[2] Paterson, MS, Wong T-F. Experimental rock deformation – the brittle field. Springer, Berlin-Heidelberg, 2005.

[3] Mogi K. Experimental rock mechanics. Geomechanics Research Series 3. Taylor & Francis Group, London, 2007.

[4] Chang C, Zoback MD, Khaksar A. Empirical relations between rock strength and physical properties in sedimentary rocks. J Petr Sci Eng 2006;51:223-37.

[5] Potyondy DO, Cundall PA. A bonded-particle model for rock. Int J Rock Mech Min Sci 2004;41:1329-64.

[6] Cundall PA. A discontinuous future for numerical modelling in geomechanics? Geotech Eng 2001;149:41-47.

[7] Savage, JC, Byerlee JD, Lockner DA. Is internal friction friction? Geophy. Res Let 1996;23:487-90.

[8] Colmenares LB, Zoback MD. A statistical evaluation of intact rock failure criteria constrained by polyaxial test data for five different rocks. Int J Rock Mech Min Sci 2002;39:695-729.

[9] Ramsey JM, Chester FM. Hybrid fracture and the transition from extension fracture to shear fracture. Nature 2004;428:63-66.

[10] Engelder T. Transitional-tensile fracture propagation: a status report. J Struct Geol 1999;21:1049-55.

[11] Vernik L, Bruno M, Bovberg C. Empirical relations between compressive strength and porosity of siliciclastic rocks. Int J Rock Mech Min Sci 1993;30:677-80.

[12] Bell FG, Lindsay P. The petrographic and geomechanical properties of some sandstones from the Newspaper Member of the Natal Group near Durban, South Africa. Eng Geol 1999;53:57-81.

[13] Palchik V. Influence of porosity and elastic modulus on uniaxial compressive strength in soft brittle porous sandstones. Rock Mech Rock Engng 1999;32:303-09.

[14] Palchik V. Application of Mohr–Coulomb failure theory to very porous sandy shales. Int J Rock Mech Min Sci 2006;43:1153-62.

[15] Rosengren KJ, Jaeger JC. The mechanical properties of an interlocked low-porosity aggregate. Géotechnique 1968;18:317-26.

[16] Mahmutoglu Y. Mechanical behaviour of cyclically heated fine grained rock. Rock Mech Rock Eng 1998;31:169-79.

[17] PFC3D (Particle Flow Code in Three Dimensions). Version 3.1. Minneapolis: Itasca Consulting Group, 2005.

[18] Abe S, Place D Mora P. A parallel implementation of the lattice solid model for the simulation of rock mechanics and earthquake dynamics. PAGEOPH 2004;161:2265-77.

[19] Wang Y, Abe S, Latham S, Mora P. Implementation of particle-scale rotation in the 3-D Lattice Solid Model. PAGEOPH 2006;163:1769-85.

[20] Thornton C. Numerical simulations of deviatoric shear deformation of granular media. Géotechnique 2000;50:43-53.

[21] Boutt DF, McPherson BJOL. Simulation of sedimentary rock deformation: Lab-scale model calibration and parameterization. Geophys Res Lett 2002;29:1054.

[22] Cho N, Martin CD, Sego DC. A clumped particle model for rock. Int J Rock Mech Min Sci 2007;44:997-1010.

[23] Ting JM, Khwaja M, Meachum LR, Rowell JD. An ellipse-based discrete element model for granular materials. Int J Numer Anal Methods Geomech 1993;17:603–23.

[24] Iwashita K, Oda M. Rolling resistance at contacts in simulation of shear band development by DEM. J Engrg Mech 1998;124:285-92.

[25] Egholm DL. A new strategy for discrete element numerical models: 1. Theory. J Geophys Res 2007;112:B05203.

[26] Fakhimi A. Application of slightly overlapped circular particles assembly in numerical simulation of rocks with high friction angles. Eng Geol 2004;74:129-38.

[27] Bagi K. An algorithm to generate random dense arrangements for discrete element simulations of granular assemblies. Granular Matter 2005;7:31-43.

[28] Place D, Mora P. A random lattice solid model for simulation of fault zone dynamics and fracture process. In: Bifurcation and Localisation Theory in Geomechanics, Balkema Rotterdam/Brookfield, 2001.

[29] Bobich JK. Experimental analysis of the extension to shear fracture transition in Berea Sandstone. MSc thesis, Dept of Geol & Geophys, University of Texas at Austin, 2005.

[30] Mogi K. Effect of intermediate principal stress on rock failure. J Geophys Res 1967;72:5117-31.

[31] Faulkner DR, Mitchell TM, Healy D, Heap MJ. Slip on 'weak' faults by the rotation of regional stress in the fracture damage zone. Nature 2006;444:922-25.

[32] Avar BB, Hudymab N, Karakouziana M. Porosity dependence of the elastic modulus of lithophysae-rich tuff: numerical and experimental investigations. Int J Rock Mech Min Sci 2003;40:919-28.

[33] Yoon J. Application of experimental design and optimization to PFC model calibration in uniaxial compression simulation. Int J Rock Mech Min Sci 2007;44:871-889.

[34] Wong T-F, David C, Zhu W. The transition from brittle faulting to cataclastic flow in porous sandstones: Mechanical deformation. J Geophys Res 1997;102:3009-25.

[35] Fairhurst C. On the validity of the 'Brazilian' test for brittle materials. Int J Rock Mech Min Sci 1964;1:535-546.

Figure captions

Fig. 1. Failure envelopes and rock property relations of siliciclastic rocks. (a) Peak stress data obtained from triaxial extension tests on Berea sandstone at various confining pressures plotted in principal stress diagram. (b) Data shown in (a) together with results from triaxial compression tests on Berea sandstone plotted on a maximum shear stress vs mean stress diagram. Best-fit parabolic Mogi 1967 failure criterion [30] is shown (Texas A&M data from Ref. 29, Wong et al. data from Ref. 34). (c) Strength at various confining pressure (labelled curves), (d) friction angle and (e) Young's modulus vs porosity for Donetsk sandstone (data in (c) and (d) from Ref. 14, and data in (e) from Ref. 13). (f) Unconfined compressive and tensile strength (UCS and T, respectively), (g) UCS/T and (h) Young's modulus vs number of heating cycles for Buchberger sandstone (data from Ref. 16).

Fig. 2. PFC3D models used in this study. The two end-member models (i and ii) are comprised of ~27,000 particles and their particle size distributions are shown in Fig. 3.

Fig. 3. Plot of cumulative number of particles vs particle radius normalised to the sample width for the two end-member models (framed in Fig. 2).

Fig. 4. Stress difference and volumetric strain vs axial strain curves obtained from triaxial compression tests at different confining pressures. Plots in left column are for high porosity end-member (model i in Fig. 2) and the plots in the right column are for low porosity end-member (model ii in Fig. 2). Model results in the first row were

obtained from fully bonded models, results in second row from models with half of the particle-particle contacts bonded, and results in third row from non-bonded models. The open dots are the peak stress values which were used for constructing the failure envelopes shown in Fig. 7.

Fig. 5. (a) Young's modulus and (b) Poisson's ratio vs confining pressure obtained from the slopes of the stress-strain curves shown in Fig. 4a and d (fully bonded models). Open and filled symbols are data from low and high porosity models, respectively. Elastic properties were determined at an axial strain of a tenth of the strain at peak stress. Circles and squares denote tangent and secant moduli, respectively. The dashed horizontal lines in each graph are the elastic property values obtained from the uniaxial strain tests.

Fig. 6. Stress difference and volumetric strain vs axial strain curves obtained from unconfined compression tests on the models shown in the (a) first and (b) second row of Fig. 2. Open dots are peak stress values, which are plotted vs porosity in Fig. 10a.

Fig. 7. (a and b) Failure envelopes of the two end-member models (framed in Fig. 2) in principal stress diagrams, and (c) friction angle (obtained from the slopes of triaxial compression failure envelopes) vs average confining pressure. Labels ranging from 10 to 50 are percentages of non-bonded contacts. For clarity envelopes obtained from triaxial extension tests are cut off at the σ_1 axis. The misfit between the triaxial extension and triaxial compression envelopes is due to a σ_2 dependence of strength.

Fig. 8. Data shown in Fig. 7 plotted in maximum shear stress vs mean stress diagrams (same line styles as in Fig. 7) for (a) a power-law PSD material with 23% porosity and (b) a uniform PSD material with 37% porosity. Labels ranging from 10 to 50 are percentages of non-bonded contacts. The curves are best-fit parabolic functions that were obtained using a least-square regression and by systematically varying the β-value given in Eq. (3).

Fig. 9. (a) Unconfined compressive and tensile strength (UCS and T, respectively), (b) UCS/T, and (c) elastic properties vs percentage of non-bonded contacts. Keys to the curves are shown: the numbers followed by a *k* (= thousand) is the approximate number of particles comprising the models, and ϕ is the porosity. LdB are UCS/T data from PFC3D models of cylindrical specimens of Lac du Bonnet granite provided by David Potyondy (microproperties given in Ref. 5).

Fig. 10. Plots of (a) unconfined compressive and tensile strength (UCS and T, respectively), (b) UCS/T, (c) friction angle, and (d) elastic properties vs porosity. Data in (a, b and d) were obtained from fully bonded materials and data in (c) from non-bonded materials (using the same range of confining pressure as in Fig. 7c). The bars in (c) indicate the range of internal friction angles obtained for fully bonded materials (Fig. 7c); arrows point towards increasing confinement. ESyS models (UCS/T data in b) with various porosities were generated by varying the particle size range for the particle insertion method (see text for details).

Fig. 11. Chart summarizing some of the mechanical property relations obtained in this study. σ = stress/strength, ε = strain, P = confining pressure, E = Young's modulus, ν

= Poisson’s ratio, φ = friction angle, and ρ_{crks} = ‘crack density’ or percentage of non-bonded contacts. Solid curves are for fully or partially bonded materials, dashed curves for non-bonded materials. The graphs are selected results from Figs. 4, 5, 7 and 9. See text for further explanation.

Table 1

PFC3D microproperties

Symbol	Description[a]	Value
E_c, GPa	Young's modulus of particles	50
k_n / k_s	ratio of particle normal to shear stiffness	2.5
μ_c	particle contact friction coefficient	0.5
$\bar{E}_c$, GPa	cement (i.e. bond) modulus	50
$\bar{k}_n / \bar{k}_s$	ratio of bond normal to shear stiffness	2.5
$\bar{\sigma}_c$, MPa	average tensile bond strength (standard deviation)	100 (20)
$\bar{\tau}_c$, MPa	average shear bond strength (standard deviation)	100 (20)
λ	bond width multiplier	1

[a] Definition of microproperties and modulus-stiffness scaling relations are given in Ref 5.

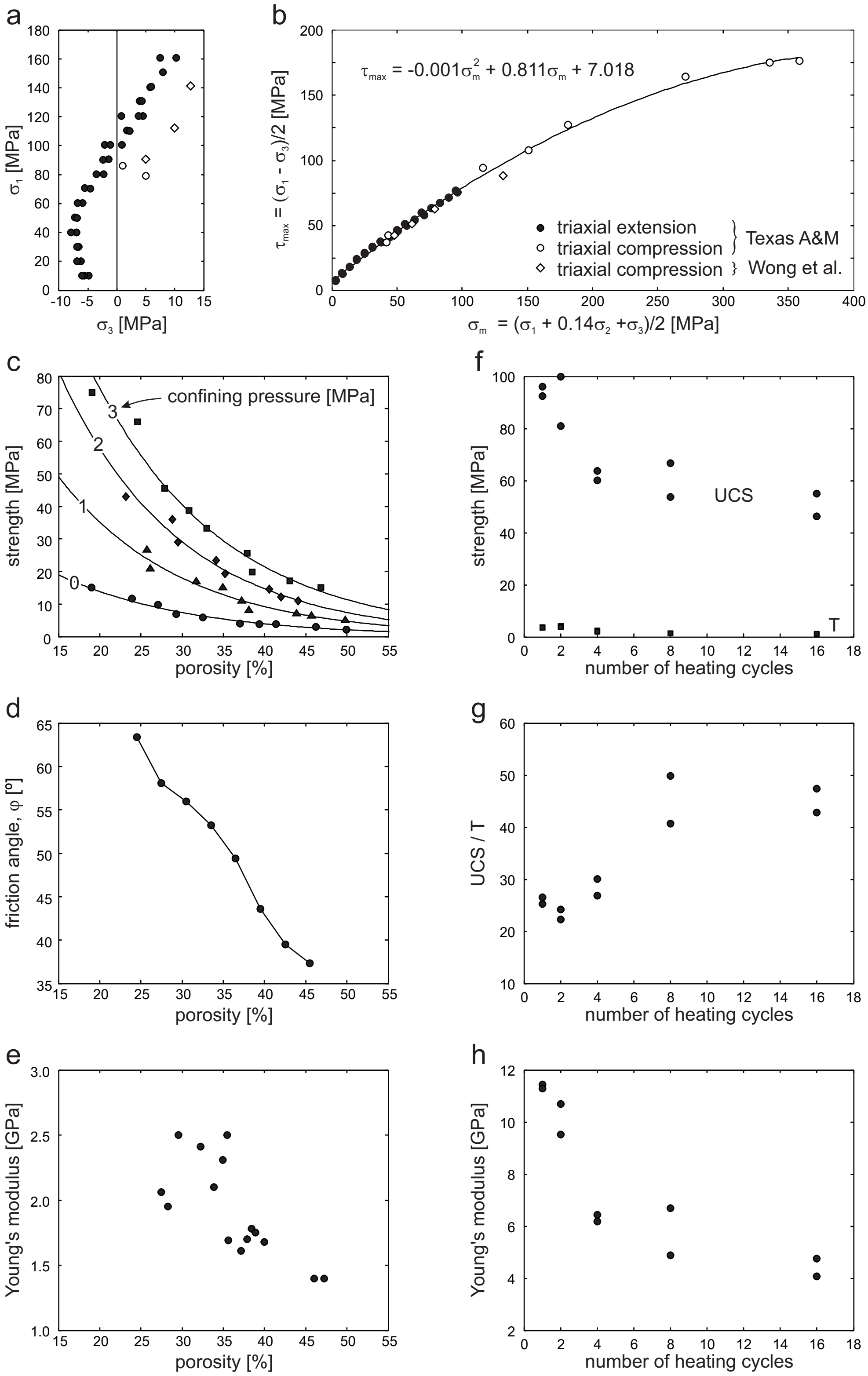

a
b
c
d
e
f
g
h
σ1 [MPa]
σ3 [MPa]
τmax = -0.001σm² + 0.811σm + 7.018
τmax = (σ1 - σ3)/2 [MPa]
σm = (σ1 + 0.14σ2 +σ3)/2 [MPa]
triaxial extension
triaxial compression
triaxial compression
Texas A&M
Wong et al.
confining pressure [MPa]
strength [MPa]
porosity [%]
friction angle, φ [º]
Young's modulus [GPa]
number of heating cycles
UCS
T
UCS / T

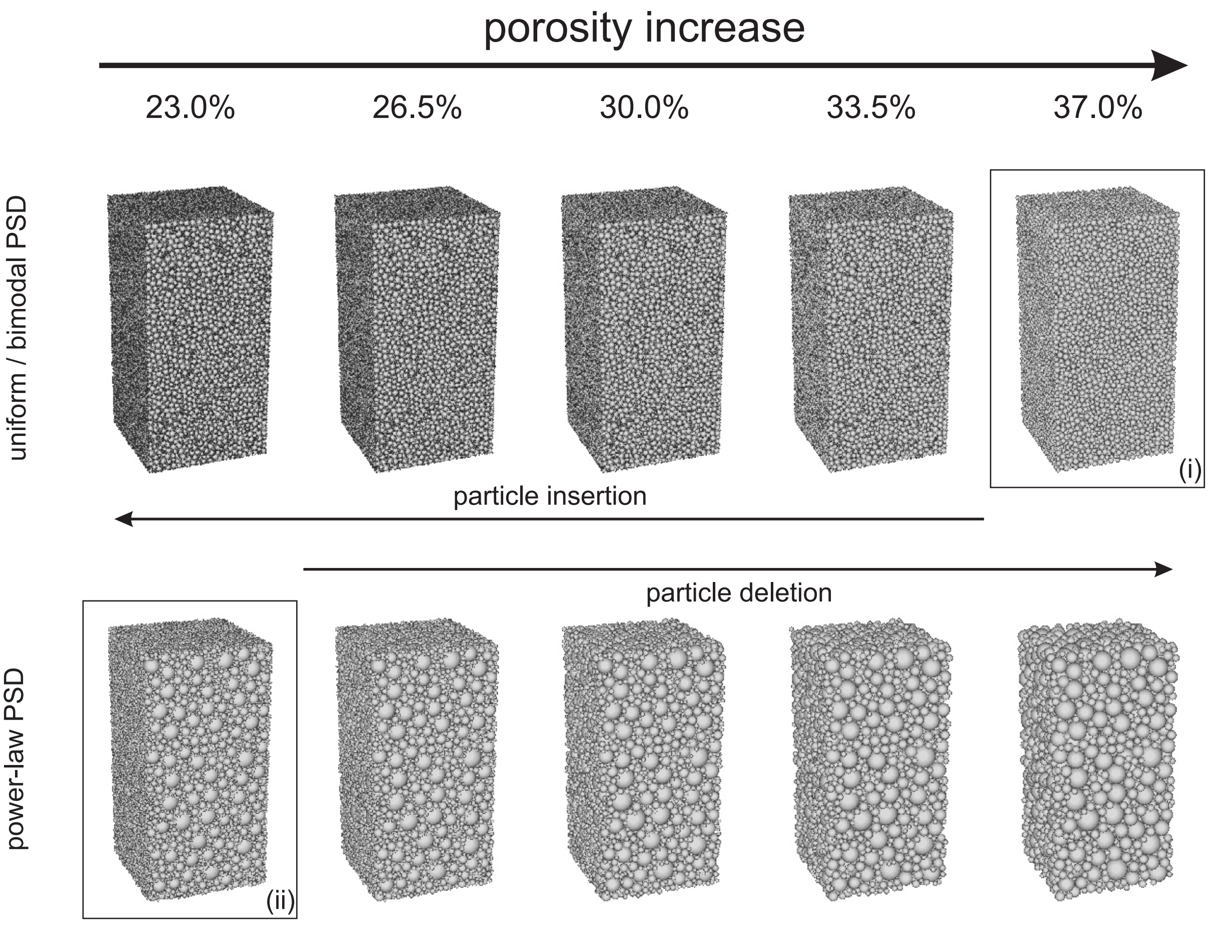
porosity increase
23.0%
26.5%
30.0%
33.5%
37.0%
uniform / bimodal PSD
(i)
particle insertion
particle deletion
power-law PSD
(ii)

Figure 2

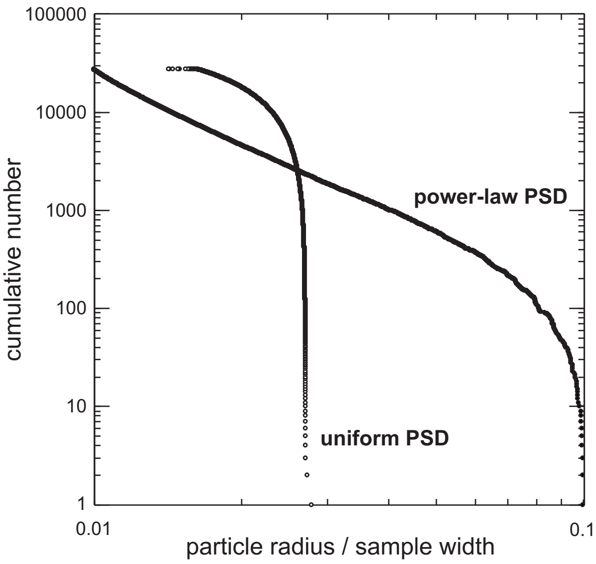
100000
10000
1000
100
10
1
0.01
0.1
cumulative number
particle radius / sample width
power-law PSD
uniform PSD

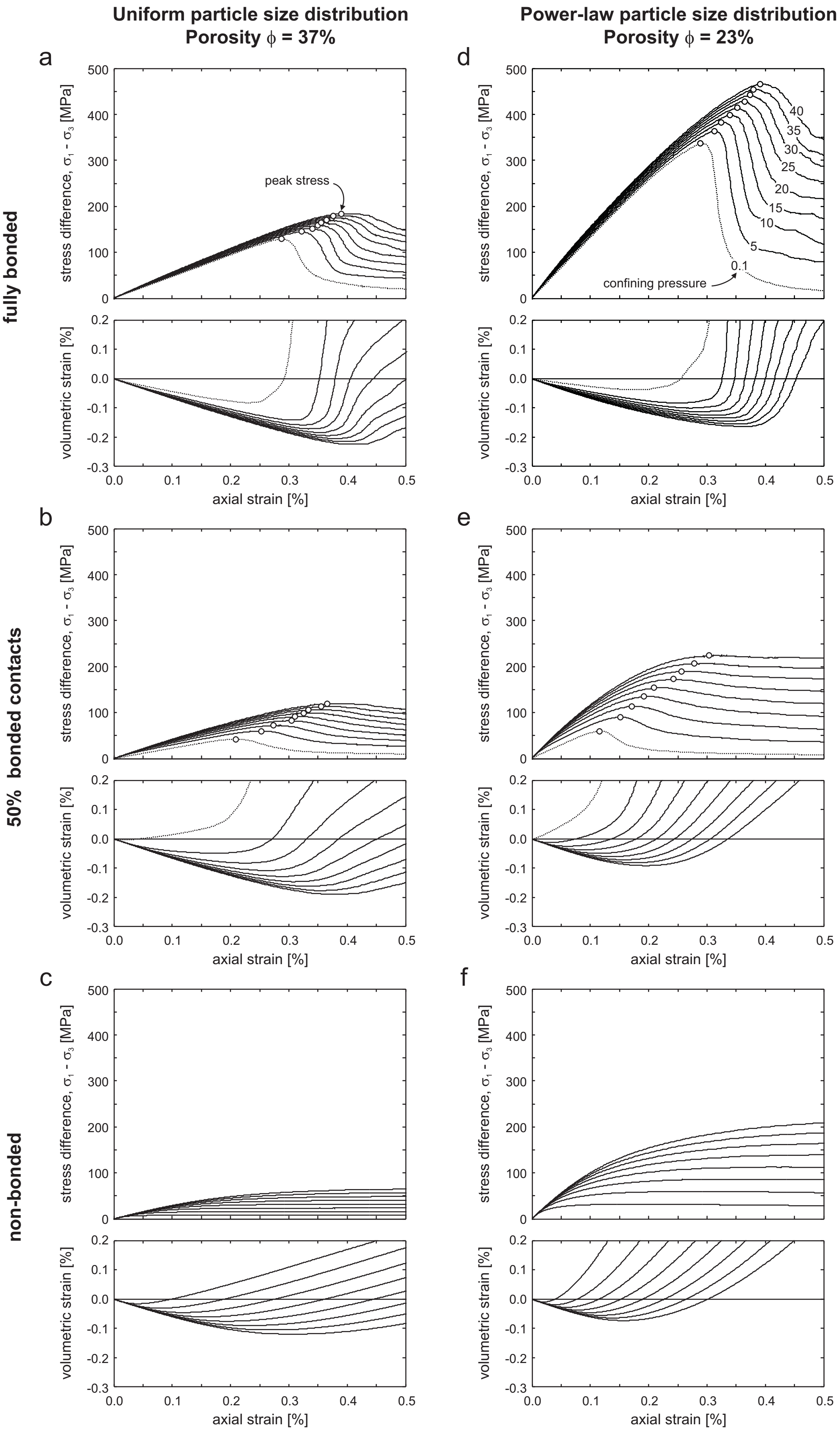

Uniform particle size distribution
Porosity φ = 37%
Power-law particle size distribution
Porosity φ = 23%
a
b
c
d
e
f
fully bonded
50% bonded contacts
non-bonded
stress difference, σ1 - σ3 [MPa]
volumetric strain [%]
axial strain [%]
peak stress
confining pressure
0.1
5
10
15
20
25
30
35
40

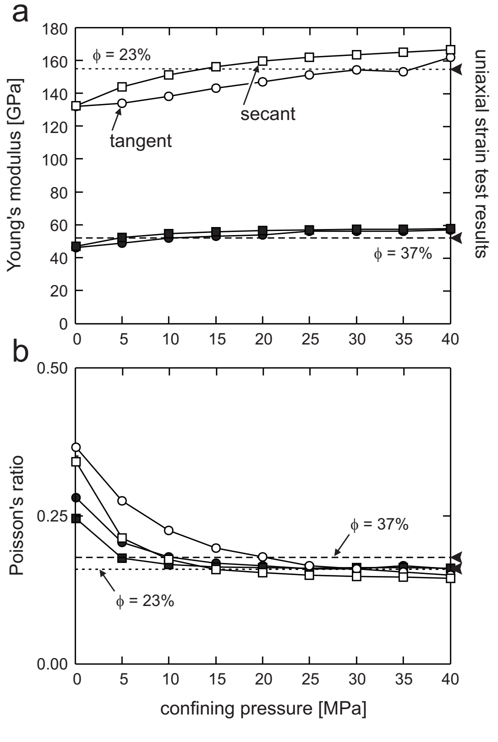

a
Young's modulus [GPa]
180
160
140
120
100
80
60
40
20
0
φ = 23%
tangent
secant
φ = 37%
uniaxial strain test results
0
5
10
15
20
25
30
35
40
b
Poisson's ratio
0.50
0.25
0.00
φ = 37%
φ = 23%
confining pressure [MPa]

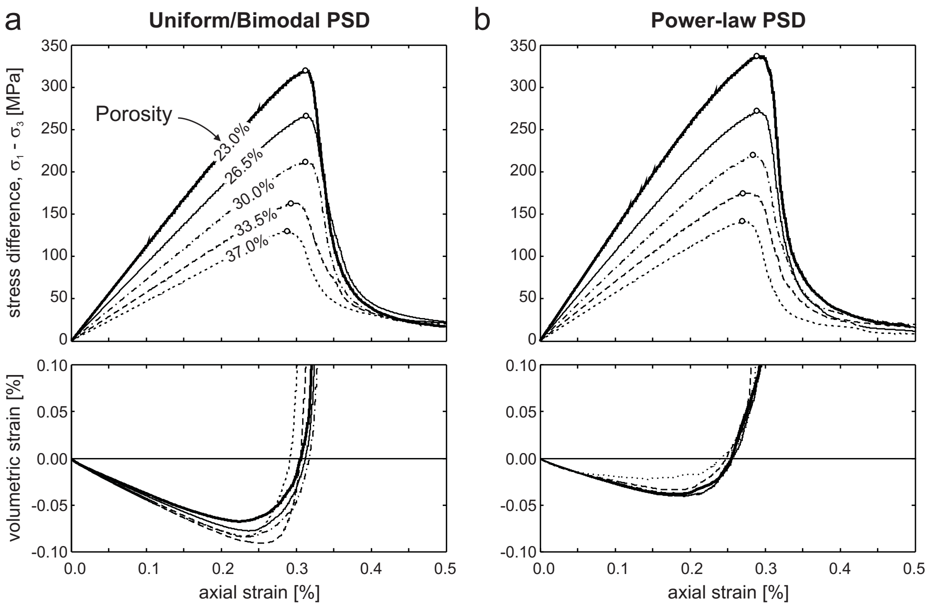

a
Uniform/Bimodal PSD
b
Power-law PSD
stress difference, σ1 - σ3 [MPa]
Porosity
23.0%
26.5%
30.0%
33.5%
37.0%
volumetric strain [%]
axial strain [%]

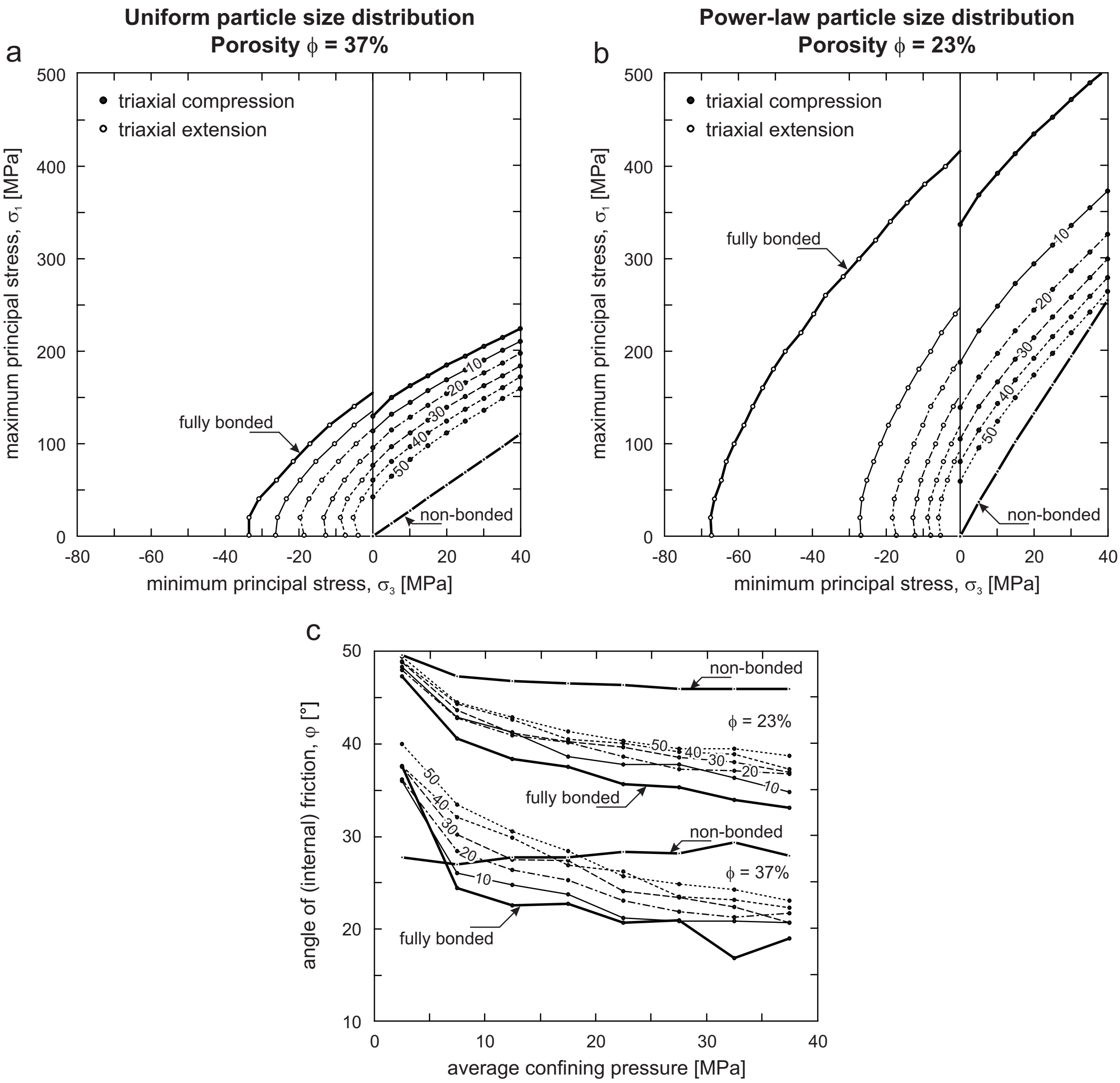
Uniform particle size distribution
Porosity ϕ = 37%
a
triaxial compression
triaxial extension
fully bonded
non-bonded
maximum principal stress, σ1 [MPa]
minimum principal stress, σ3 [MPa]
Power-law particle size distribution
Porosity ϕ = 23%
b
triaxial compression
triaxial extension
fully bonded
non-bonded
maximum principal stress, σ1 [MPa]
minimum principal stress, σ3 [MPa]
c
non-bonded
ϕ = 23%
fully bonded
non-bonded
ϕ = 37%
fully bonded
angle of (internal) friction, φ [°]
average confining pressure [MPa]

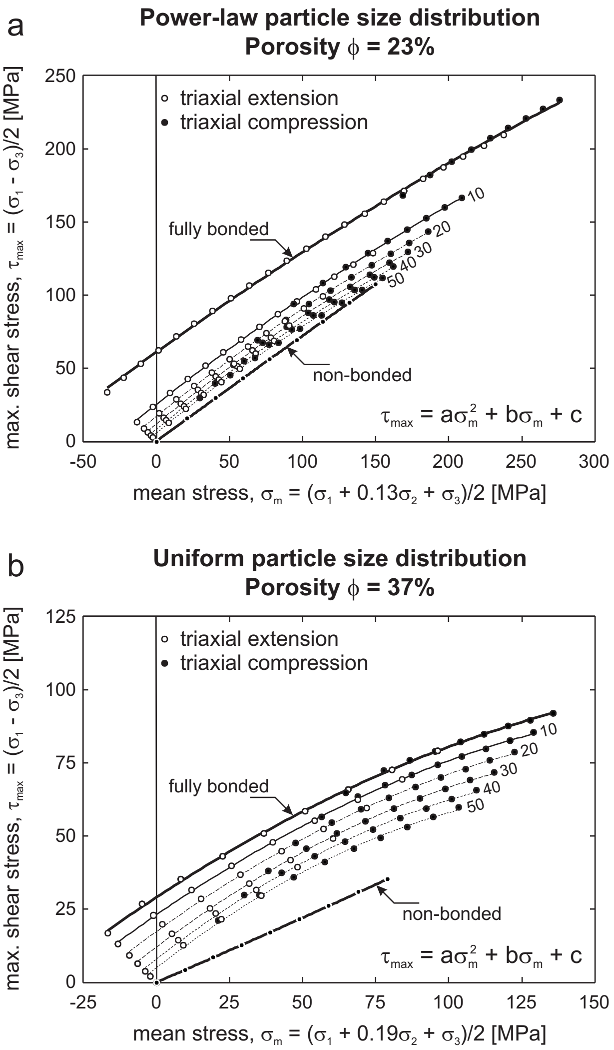
a
Power-law particle size distribution
Porosity ϕ = 23%
triaxial extension
triaxial compression
fully bonded
non-bonded
10
20
30
40
50
$\tau_{max} = a\sigma_m^2 + b\sigma_m + c$
max. shear stress, $\tau_{max} = (\sigma_1 - \sigma_3)/2$ [MPa]
mean stress, $\sigma_m = (\sigma_1 + 0.13\sigma_2 + \sigma_3)/2$ [MPa]
b
Uniform particle size distribution
Porosity ϕ = 37%
triaxial extension
triaxial compression
fully bonded
non-bonded
10
20
30
40
50
$\tau_{max} = a\sigma_m^2 + b\sigma_m + c$
max. shear stress, $\tau_{max} = (\sigma_1 - \sigma_3)/2$ [MPa]
mean stress, $\sigma_m = (\sigma_1 + 0.19\sigma_2 + \sigma_3)/2$ [MPa]

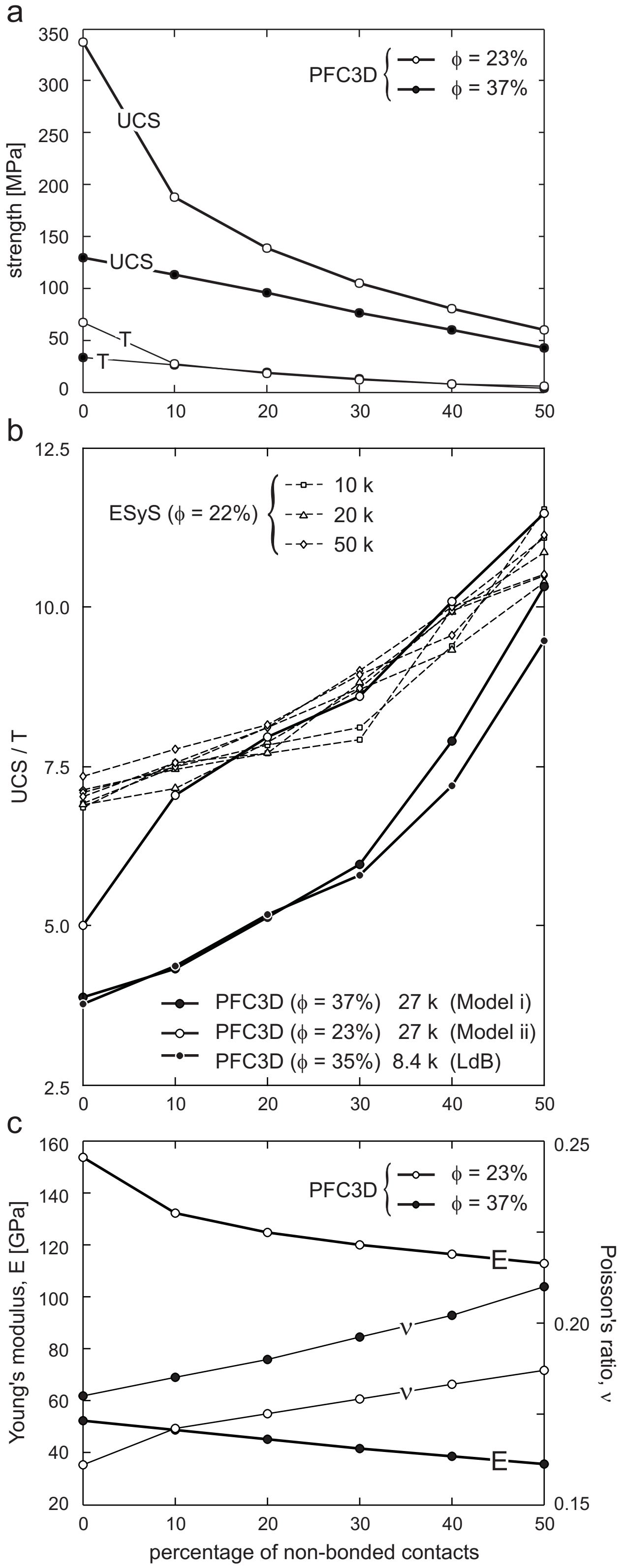

a
PFC3D
ϕ = 23%
ϕ = 37%
UCS
UCS
T
T
strength [MPa]
b
ESyS (ϕ = 22%)
10 k
20 k
50 k
UCS / T
PFC3D (ϕ = 37%) 27 k (Model i)
PFC3D (ϕ = 23%) 27 k (Model ii)
PFC3D (ϕ = 35%) 8.4 k (LdB)
c
PFC3D
ϕ = 23%
ϕ = 37%
E
ν
ν
E
Young's modulus, E [GPa]
Poisson's ratio, ν
percentage of non-bonded contacts

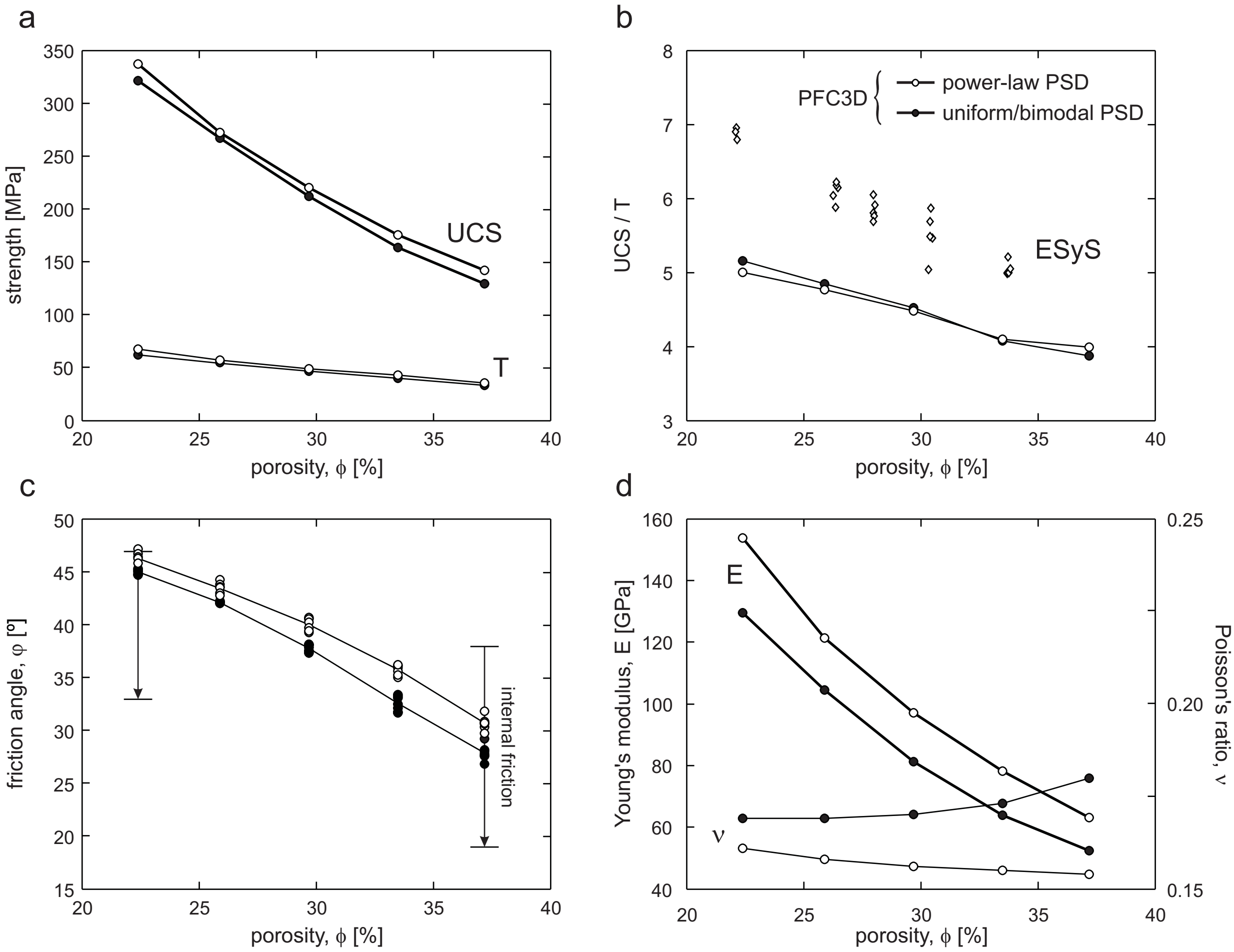

a
strength [MPa]
UCS
T
porosity, ϕ [%]
b
UCS / T
PFC3D
power-law PSD
uniform/bimodal PSD
ESyS
porosity, ϕ [%]
c
friction angle, φ [º]
internal friction
porosity, ϕ [%]
d
Young's modulus, E [GPa]
Poisson's ratio, ν
E
ν
porosity, ϕ [%]

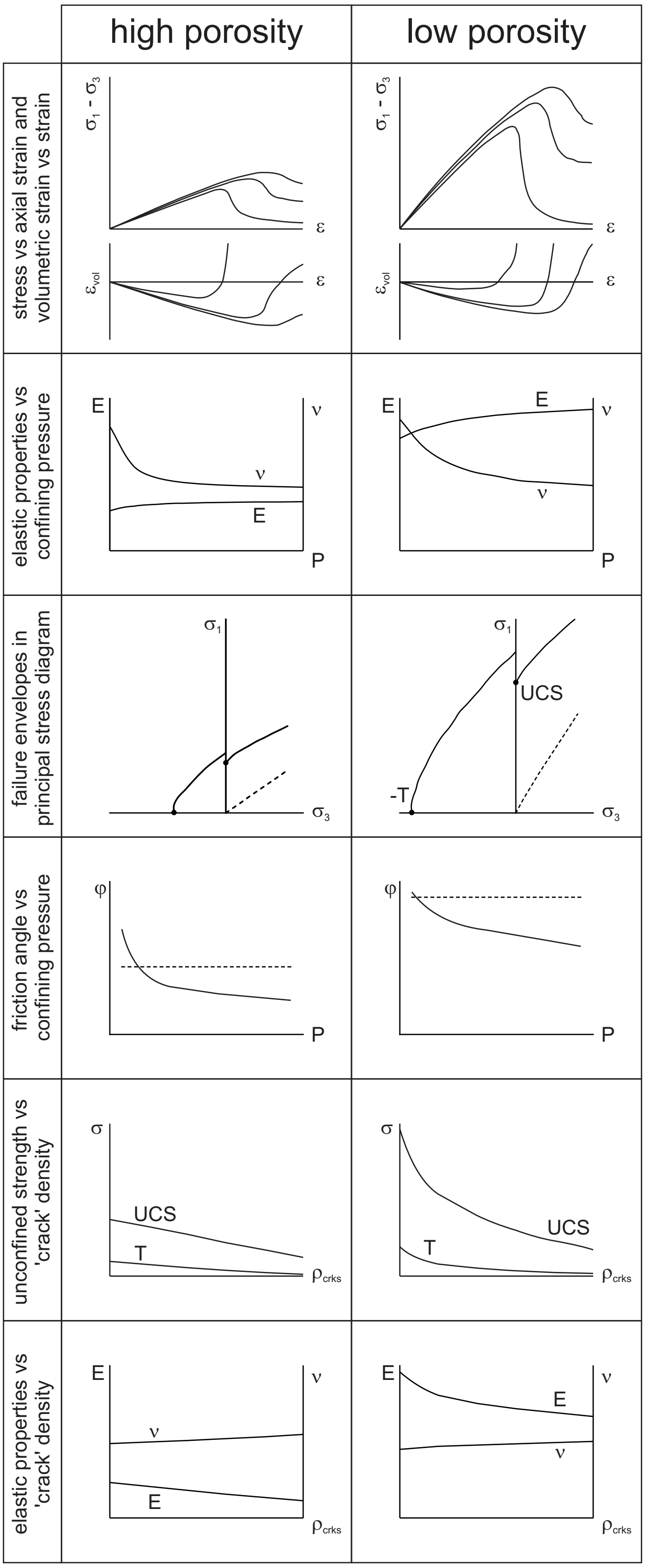

high porosity
low porosity
stress vs axial strain and volumetric strain vs strain
elastic properties vs confining pressure
failure envelopes in principal stress diagram
friction angle vs confining pressure
unconfined strength vs 'crack' density
elastic properties vs 'crack' density
$\sigma_1 - \sigma_3$
ε
ε_{vol}
E
ν
P
σ_1
σ_3
UCS
-T
φ
σ
T
ρ_{crks}

Figure 11